Piezoelectric properties of 3-*X* periodic $Pb(Zr_xTi_{1-x})O_3$–polymer composites

James E. Smay
Department of Materials Science and Engineering, University of Illinois at Urbana-Champaign, Urbana, Illinois 61801 and Sandia National Laboratories, Albuquerque, New Mexico 87106

Joseph Cesarano III and Bruce A. Tuttle
Sandia National Laboratories, Albuquerque, New Mexico 87106

Jennifer A. Lewis[a)]
Department of Materials Science and Engineering, University of Illinois at Urbana-Champaign, Urbana, Illinois 61801

(Received 22 March 2002; accepted 19 August 2002)

The piezoelectric properties of lead zirconate titanate (PZT)–polymer composites were studied as a function of composition and phase connectivity. PZT skeletal structures were fabricated by robotic deposition, densified at 1275 °C, and subsequently infiltrated with epoxy to produce the desired PZT–polymer composites. These 3-*X* structures consisted of a three-dimensional lattice of PZT rods (3–3) embedded in a polymer matrix, a PZT lattice/polymer matrix capped with PZT face plates (3–2), or PZT lattice/polymer matrix capped with PZT face plates and encircled by a solid PZT ring (3–1). The PZT:polymer ratio was varied systematically by changing the lattice (rod) spacing in each composite architecture. The concentration of PZT pillars, which formed along the poling direction at the intersections between PZT rods, varied as the PZT volume fraction squared. These 3-*X* composites displayed enhanced hydrostatic figures of merit relative to monolithic PZT due to stress concentration in the PZT pillars and their dramatically reduced dielectric constant, with the highest values found for the 3–2 and 3–1 composites. Our experimental observations were compared to theoretical predictions based on an isostrain, unit cell model modified to account for the partial support of stress in the stiff epoxy phase. © *2002 American Institute of Physics.*
[DOI: 10.1063/1.1513202]

I. INTRODUCTION

Lead zirconate titanate (PZT)–polymer composites are widely used in hydrophone and ultrasonic imaging applications.[1–4] Their superior performance over monolithic PZT stems from the connectivity[1,5,6] and macrosymmetry[1] of stiff, high permittivity PZT elements in a compliant, low permittivitty polymer matrix. Such structures are designed to redirect the stress and flux patterns into the continuous PZT phase (or pillars) aligned along the poling direction. The presence of the polymer phase not only promotes this, but simultaneously reduces the dielectric constant and density thereby enhancing the voltage output and lowering its acoustic impedance, respectively. The largest hydrostatic figures of merit for simple, diphasic PZT-polymer composites[2] have been obtained with 3-*X* type structures (i.e., 3–3,[7–9] 3–2,[10] and 3–1[10,11]), where the first number represents the PZT connectivity and the latter the polymer connectivity.

3-*X* type PZT-polymer composites were originally formed by creating skeletal ceramic structures using a replamine process[7] and later by volatilizing fugitive species from a powder compact,[8,9] partial sintering,[12] and infiltrating polymer foam as templates.[13] Such techniques resulted in poorly controlled composite architectures with tortuous, interpentrating PZT, and polymer networks. More recently, PZT structures have been formed by drilling holes in PZT blocks,[10] extrusion,[11,14] lamination of tape-cast layers,[15] and manually stacking sintered PZT bars.[16] While these techniques offer improved control over the composite architecture, they are laborious and limited to certain designs.

Direct-write techniques[17–29] offer a facile route for producing complex three-dimensional structures required for piezoelectric composite applications. Here, we demonstrate this approach by fabricating a broad array of 3-*X* composites via a robotic deposition technique known as robocasting.[23,24] Concentrated colloidal inks were used to directly assemble PZT skeletal structures with self-supporting spanning elements and continuous features such as solid face plates and rings. We present a systematic study of the dielectric and piezoelectric properties as a function of PZT: polymer ratio and architecture for composites produced by this direct-write approach. Our experimental observations were compared to theoretical predictions based on an isostrain model that was modified to account for the partial support of stress in the stiff epoxy phase. The addition of solid face plate and ring elements was shown to enhance the performance of these thin (~1 mm) composite structures by mitigating nonuniformities in their surface displacement.[30,31]

a)Electronic mail: jalewis@uiuc.edu

II. EXPERIMENTAL PROCEDURE

A. Materials system

The piezoelectric phase was produced from a lead zirconate titanate powder, PZT–5H (Morgan Matroc Inc., Electro Ceramics Division, Bedford, OH). The PZT powder had an average particle diameter of 0.67 μm, a density of 7.6 g/cm^3, a specific surface area of 1.86 m^2/g, and ~0.3 wt % poly(acrylic acid) preadsorbed as a dispersant. A vinylcyclohexene dioxide epoxy (Spurrs Epoxy, Polysciences Inc., Warrington, PA) served as the passive polymer phase. Concentrated colloidal gel-based inks were formulated by suspending the as-received PZT particles in an aqueous solution of 0.5 wt % cellulose (Methocel F4M, Dow Chemical Co., Midland, MI) at pH~9. Upon decreasing the ink pH~6.5 through titration using a 1 M HNO_3 solution, an attractive particle network formed via colloidal gelation.[32–37] Further details regarding ink design and rheological properties are provided in Smay *et al.*[38]

B. Robotic deposition of PZT-polymer composites

PZT-polymer composites were fabricated by first assembling PZT skeletal structures by robocasting, followed by sintering and infiltration with the polymer. This direct-write technique employed an ink delivery system mounted on a z-axis motion stage for agile printing onto a moving x-y stage. A custom-designed, computer-aided direct-write program (RoboCAD 2.0) allowed for the construction of complex, three-dimensional architectures in a layer-by-layer deposition scheme. Any conceivable 2D pattern may be printed within a layer, which then serves as a platform for the deposition of subsequent layers. The layers had a finite thickness ($\Delta z = 0.82D$) defined by the height change of the deposition nozzle from layer to layer. The cross-sectional area of the deposited rods was determined by the nozzle diameter ($D = 200$ μm). For these composites, lattice structures were assembled by depositing periodic arrays of rods of varying spacing in each layer with a 90° rotation between layers.

The PZT skeletal structures were dried for 20 min in a 70 °C oven followed by bisque firing at 700 °C for 1 h. Upon cooling, the skeletons were placed on a PZT setter plate, enclosed in an alumina crucible with a PZT powder bed for atmosphere control, and sintered at 1275 °C for 2 h. Their sintered density was evaluated by the Archimides method.[39] Infiltration of these PZT lattices was accomplished by immersing them in a pool of epoxy resin under light vacuum to promote removal of entrained air from the lattice interior. The vacuum was removed and the epoxy was allowed to cure overnight at 70 °C.

Schematic illustrations of 3–3, 3–2, and 3–1 PZT skeletal structures are shown in Fig. 1, with a wedge shaped cutout to reveal their interior structure. The 3–3 composites consisted of a ten-layer PZT lattice where each layer was deposited as an array of parallel rods inside a circular perimeter ring. After sintering and polymer infiltration, the perimeter ring was removed by grinding. The 3–2 composites consisted of a 14-layer design where two extra layers were added both beneath and on top of a ten-layer lattice structure. These extra layers consisted of a concentric PZT disk, radially filled transition region that allowed for polymer infiltration, and a perimeter ring. After sintering and polymer infiltration, the ring and transition region were removed by grinding, leaving behind a lattice sandwiched between face plates of PZT. The 3–1 composites were formed with the same scheme as 3–2 composites, but the perimeter ring and transition region were left intact. The PZT volume fraction (ϕ_{PZT}) in the lattice region of each structure is proportional to the ratio of rod diameter (D) to spacing (L). For 3–3 composites, L was varied from 300 to 1200 μm resulting in ϕ_{PZT} from 0.17 to 0.70. For the 3–2 and 3–1 composites, L was varied from 350 to 750 μm yielding ϕ_{PZT} from 0.28 to 0.60. In addition to composite structures, monolithic PZT–5H disks were fabricated by robocasting and by cold isostatic pressing (CIP) at 200 MPa, which served as a benchmark for the observed behavior.

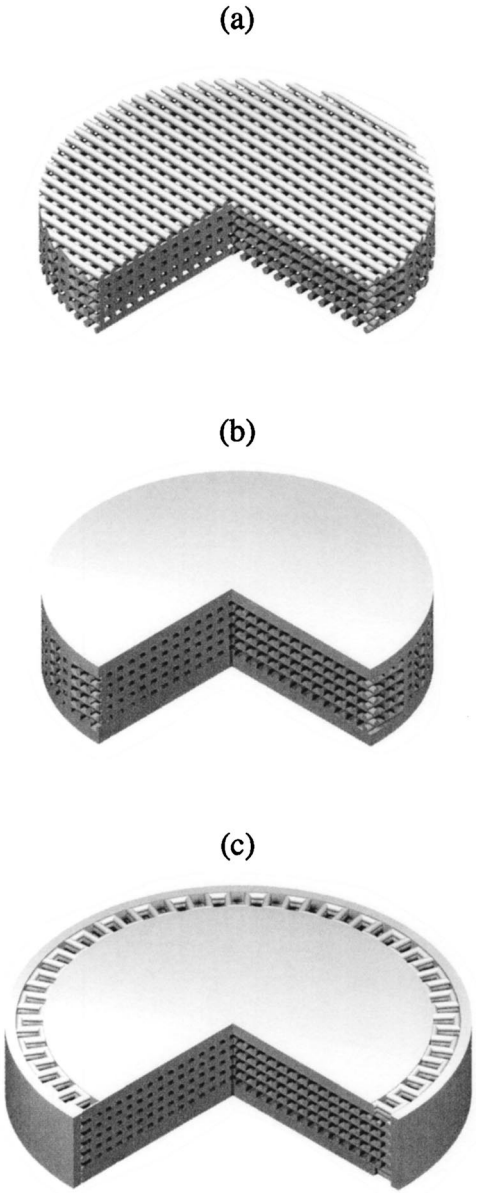

FIG. 1. Schematic illustrations of (a) 3–3, (b) 3–2, and (c) 3–1 PZT skeletons with a cutout section to reveal the internal structure. The 3–3 and 3–2 skeletons are illustrated without the PZT ring that aided in handling the green structures.

TABLE I. Materials parameters.

	s_{33} (10^{-12} Pa^{-1})	s_{11} (10^{-12} Pa^{-1})	d_{33} (10^{-12} pC/N)	d_{31} (10^{-12} pC/N)	K_3
PZT	18	16	593	−274	3400
Epoxy	143	143	0	0	4

C. Characterization of PZT–polymer composites

Both PZT–polymer composites and monolithic PZT disks were polished and electroded by gold sputtering. All samples were poled at 25 kV/cm for 30 min at room temperature followed by short circuiting for 1 h to accelerate aging. The dielectric constant (K_3) and tan δ of the composites and solid disks were measured with an impedance analyzer (HP 4284A precision LCR meter, Yakogama-Hewlett-Packard, Tokyo, Japan) at a frequency of 1 kHz and field strength of 1 V/mm. The piezoelectric d_{33} coefficient was measured with a Berlincourt meter (Model CPDT3300, Channel Industries Inc., Santa Barbara, CA) using hemispherical contacts. Several readings were taken across the composite surface and the values were averaged. Finally, the hydrostatic piezoelectric coefficient (d_h) was characterized by a low frequency oscillatory pressure technique. The samples were immersed in pressure transfer fluid (Isopar H) and a 0.76 MPa (110 psi) offset pressure applied. The pressure was then cycled at 0.2 Hz from 0.76 to 0.62 MPa (90 psi) and the current output of the test sample was compared to a standard, yielding the hydrostatic piezoelectric coefficient.

III. MODELING OF 3-*X* PZT–POLYMER COMPOSITES

The improved hydrostatic performance of 3-*X* type composites relative to bulk PZT has been attributed to two factors:[1,5–10,30,31,40–46] (1) stress concentration in the stiff PZT phase resulting in a high d_{33} coefficient despite the reduction in ϕ_{PZT} and (2) reduction of the dielectric constant with decreasing ϕ_{PZT}. Parallel and series mixing rules for compliance, permittivity, and piezoelectric constant have been invoked to explain the behavior of 3–3 composites via an isostrain, unit cell model.[5,7,8] The isostrain condition assumes that equivalent deflections occur in both the PZT and polymer phases connected in parallel. In the unit-cell based approach,[9,44–46] the PZT phase is represented by a unit cell of three orthogonal bars joined at a common intersection. Previously,[7–9,44] the role of the polymer phase was neglected by assuming that only the PZT pillars support stress. Although this assumption appears reasonable for thick samples with a very compliant polymer phase, it may not be appropriate for thin composites with a relatively stiff epoxy. We therefore modified the 3-*X* models to include polymer stiffness. The materials properties listed in Table I are incorporated into Eqs. (1)–(13) and the dielectric and piezoelectric properties calculated as a function of ϕ_{PZT}. A comparison between these predicted values and those obtained experimentally is presented in the next section.

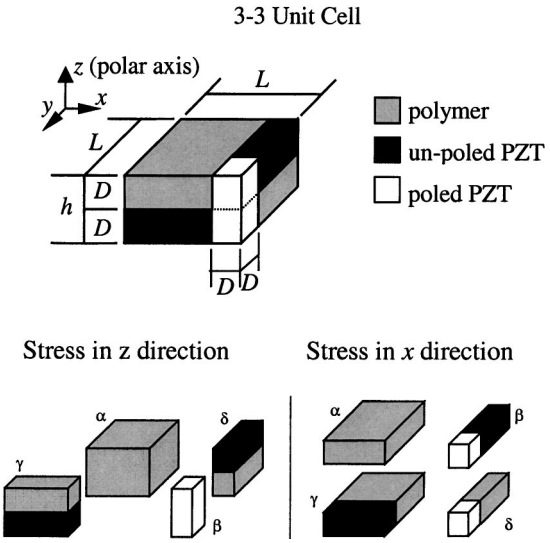

FIG. 2. Unit cell representing the key components of the 3–3 composite (i.e., polymer, PZT struts, and PZT pillars) and subdivision scheme for stress in the *x*, *y*, or *z* direction.

A. 3–3 unit-cell model

The lattice portion of the PZT–polymer composites can be represented with a simple unit cell as shown in Fig. 2. Here, the lattice rods have been idealized as rectangular beams connected at a lap joint. The width and height of the beams (D) are considered equivalent to the diameter of the rods in the real lattice structure, such that the total height of the unit cell is $2D$. The length of the beams is defined by the lattice spacing (L) and therefore the PZT volume fraction is D/L. During poling, the high permittivity pillars of PZT formed at the junctions of the lattice rods collect the electric flux and therefore are the only piezoelectric elements in the unit cell. The remaining unpoled PZT acts as struts that interconnect the pillars.

When a hydrostatic stress is applied to the unit cell, its piezoelectric response can be modeled by linear superposition of the contributions from stress applied in the longitudinal (z) and lateral (x and y) directions. The unit cell is divided into the subunits indicated in Fig. 2 for stress in the z direction. These sections are analyzed with the series mixing rules[1] listed in Table II, where the appended subscript A refers to PZT properties and B refers to polymer properties. The numerical subscripts 1, 2, and 3 refer to the *x*, *y*, and *z*

TABLE II. Iso-strain mixing rules.

Property	Series	Parallel
$\overline{s^n} = \phi_A s_A^n + \phi_B s_B^n$	$n=1$	$n=-1$
$\overline{K^n} = \phi_A K_B^n + \phi_B K_B^n$	$n=-1$	$n=1$
$\overline{d}_{33} = \dfrac{\phi_A d_{33,A} K_{3,B}^m s_{33,B}^n + \phi_B d_{33,B} K_{3,A}^m s_{33,A}^n}{\phi_A K_{3,B}^m s_{33,B}^n + \phi_B K_{3,A}^m s_{33,A}^n}$	$m=1$ $n=0$	$m=0$ $n=1$
$\overline{d}_{31} = \left(\dfrac{\phi_A d_{31,A}}{K_{3,A}^n s_{11,A}^n} + \dfrac{\phi_B d_{31,B}}{K_{3,B}^n s_{11,B}^n} \right) \overline{s}_{11}^n \overline{K}_3^n$	$n=1$	$n=0$

directions, respectively. The subunits are then mathematically reassembled with the parallel mixing rules[1] in Table II to predict the response of the composite.

Systematic application of the mixing rules leads to Eq. (1) for $\bar{d}_{33}$:

$$\bar{d}_{33}=d_{33,\mathrm{PZT}}\phi_{\mathrm{PZT}}^2\frac{\bar{s}_{33}}{s_{33,\beta}}, \tag{1}$$

where the composite compliance ($\bar{s}_{33}$) is given by

$$\bar{s}_{33}=\frac{s_{33,\gamma}s_{33,\alpha}s_{33,\beta}}{\phi_{\mathrm{poly}}^2 s_{33,\beta}s_{33,\gamma}+\phi_{\mathrm{PZT}}^2 s_{33,\alpha}s_{33,\gamma}+2(\phi_{\mathrm{PZT}}\phi_{\mathrm{poly}})s_{33,\alpha}s_{33,\beta}}, \tag{2}$$

where $s_{33,\alpha}=s_{33,\mathrm{poly}}$, $s_{33,\beta}=s_{33,\mathrm{PZT}}$, $s_{33,\gamma}=0.5(s_{33,\mathrm{poly}}+s_{11,\mathrm{PZT}})$, and ϕ_{poly} is the polymer volume fraction ($=1-\phi_{\mathrm{PZT}}$). Application of the mixing rules for permittivity leads to the composite dielectric constant ($\bar{K}_3$) as given by:

$$\bar{K}_3=\phi_{\mathrm{poly}}^2K_{3,\alpha}+\phi_{\mathrm{PZT}}^2K_{3,\beta}+2(\phi_{\mathrm{PZT}}\phi_{\mathrm{ploy}})K_{3,\gamma} \tag{3}$$

where $K_{3,\alpha}=K_{3,\mathrm{poly}}$, $K_{3,\beta}=K_{3,\mathrm{PZT}}$, and $K_{3,\gamma}=2(K_{1,\mathrm{PZT}}K_{3,\mathrm{poly}})/(K_{1,\mathrm{PZT}}+K_{3,\mathrm{poly}})$.

When stress is applied in the lateral direction, the unit cell is divided, as indicated in Fig. 2. The symmetry of the unit cell requires only one direction to be derived. Application of the appropriate mixing rules followed by recombination of the unit cell yields the $\bar{d}_{31}$ coefficient for the composite given by

$$\bar{d}_{31}=\frac{1}{2}d_{31,\mathrm{PZT}}\phi_{\mathrm{PZT}}^2\left(\frac{1}{s_{11,\beta}}+\frac{1}{s_{11,\gamma}}\right)\bar{s}_{11}, \tag{4}$$

where the lateral compliance ($\bar{s}_{11}$) is

$$\bar{s}_{11}=\frac{2s_{11,\alpha}s_{11,\beta}s_{11,\gamma}}{\phi_{\mathrm{poly}}s_{11,\beta}s_{11,\gamma}+\phi_{\mathrm{PZT}}s_{11,\alpha}s_{11,\gamma}+s_{11,\alpha}s_{11,\beta}} \tag{5}$$

where $s_{11,\alpha}=s_{11,\mathrm{poly}}$, $s_{11,\beta}=s_{11,\mathrm{PZT}}$, and $s_{11,\gamma}=(\phi_{\mathrm{PZT}}s_{11,\mathrm{PZT}}+\phi_{\mathrm{poly}}s_{11,\mathrm{poly}})$. The hydrostatic piezoelectric coefficient ($\bar{d}_h$) is calculated by summing the longitudinal and lateral contributions as given by:

$$\bar{d}_h=\bar{d}_{33}+2\bar{d}_{31}. \tag{6}$$

As with the previous models,[9,44,46] assumptions of an infinitely compliant polymer results in $\bar{d}_{33}\approx d_{33,\mathrm{PZT}}$ and $\bar{d}_{31}\approx\phi_{\mathrm{PZT}}d_{31,\mathrm{PZT}}$ so that $\bar{d}_h\approx\bar{d}_{33}$ for small ϕ_{PZT}.

B. 3–2 model

The unit cell for the 3–2 and 3–1 composites is shown in Fig. 3. The lattice portion of this unit cell is defined with the same parameters used for the 3–3 structure. A thin PZT plate has been attached, whose thickness (t) is defined by the ratio of plate thickness to lattice thickness for entire composite structure (e.g., see Fig. 3). The plate is assumed to consist of islands of poled PZT directly above the pillars in the underlying lattice due to its series connection with the polymer phase in all other regions.

The 3–2 unit cell is modeled by systematic application of the mixing rules. For stress in the longitudinal direction, the piezoelectric constant and compliance are of the same form as Eqs. (1) and (2), respectively. The compliance of sections α and γ, are given by

$$s_{33,\alpha}=\phi_{\mathrm{lattice}}s_{33,\mathrm{poly}}+\phi_{\mathrm{plate}}s_{33,\mathrm{PZT}}, \tag{7}$$

and

$$s_{33,\gamma}=(0.5\phi_{\mathrm{lattice}}+\phi_{\mathrm{plate}})s_{11,\mathrm{PZT}}+0.5\phi_{\mathrm{lattice}}s_{33,\mathrm{poly}}, \tag{8}$$

where ϕ_{lattice} is the volume fraction of the lattice portion and ϕ_{plate} is the volume fraction of the plate. The dielectric constant takes the same form as Eq. (3) and the plate has little effect on the permittivity of sections *A* and *C* because of the series connection with the polymer.

For stress in the lateral direction, the unit cell is divided into five sections for mathematical convenience, as shown in Fig. 3. The $\bar{d}_{31}$ coefficient takes the same form as Eq. (4), however the lateral compliance ($\bar{s}_{11}$) is given by

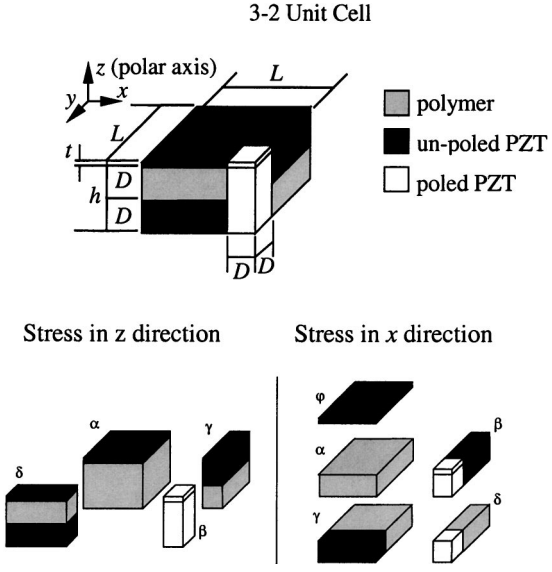

FIG. 3. 3–2 unit cell is a modification of the 3–3 unit cell (see Fig. 2) where the face plates are added as a thin slab of PZT with poled islands above the pillars. The subdivisions for stress in the *x*, *y*, or *z* direction are also shown.

$$\bar{s}_{11}=\frac{s_{11,\alpha}s_{11,\beta}s_{11,\gamma}}{\phi_\alpha s_{11,\beta}s_{11,\gamma}+(\phi_\beta+\phi_\varphi)s_{11,\alpha}s_{11,\gamma}+(\phi_\gamma+\phi_\delta)s_{11,\alpha}s_{11,\beta}}, \tag{9}$$

where the compliance coefficients are the same as in Eq. (5), $\phi_\alpha=0.5\phi_{\text{lattice}}\phi_{\text{poly}}$, $(\phi_\beta+\phi_\varphi)=0.5\phi_{\text{lattice}}\phi_{\text{PZT}}+\phi_{\text{plate}}$, and $(\phi_\beta+\phi_\varphi)=0.5\phi_{\text{lattice}}$. Thus, the PZT plate stiffens the composite in the lateral direction and reduces the magnitude of $\bar{d}_{31}$ by shielding the lattice region from stress. Rigid electrodes[40] or transverse reinforcement of the polymer by glass fibers[42] have been shown to result in similar lateral stress shielding in 1–3 composites.

C. 3–1 model

The 3–1 structure consists of three concentric sections: (1) the solid PZT ring, (2) the transition region, and (3) the 3–2 disk in the center with volume fractions ϕ_{ring}, ϕ_{trans}, and ϕ_{disk}, respectively. To avoid more complexity in the model, we assume the properties of the transition region are the same as a 3–3 lattice of similar composition. Therefore, when a longitudinal stress is applied, $\bar{d}_{33}$ is given by

$$\bar{d}_{33}=\left(\frac{\phi_{\text{ring}}d_{33,\text{PZT}}}{s_{33,\text{PZT}}}+\frac{\phi_{\text{trans}}d_{33,\text{trans}}}{s_{33,\text{trans}}}+\frac{\phi_{\text{disk}}d_{33,\text{disk}}}{s_{33,\text{disk}}}\right)\bar{s}_{33}, \tag{10}$$

where $s_{33,\text{trans}}$ and $s_{33,\text{disk}}$ are the compliances of equivalent 3–3 and 3–2 structures, respectively, and $d_{33,\text{trans}}$ and $d_{33,\text{disk}}$ are the piezoelectric coefficients of equivalent 3–3 and 3–2 structures, respectively. The longitudinal compliance ($\bar{s}_{33}$) and the dielectric constant ($\bar{K}_{33}$) are given by

$$\bar{s}_{33}=\frac{s_{33,\text{PZT}}s_{33,\text{trans}}s_{33,\text{disk}}}{\phi_{\text{ring}}s_{33,\text{trans}}s_{33,\text{disk}}+\phi_{\text{trans}}s_{33,\text{PZT}}s_{33,\text{disk}}+\phi_{\text{disk}}s_{33,\text{PZT}}s_{33,\text{trans}}}, \tag{11}$$

and

$$\bar{K}_3=\phi_{\text{ring}}K_{3,\text{PZT}}+\phi_{\text{trans}}K_{3,\text{trans}}+\phi_{\text{disk}}K_{3,\text{disk}}, \tag{12}$$

where $K_{3,\text{trans}}$ and $K_{3,\text{disk}}$ are the dielectric constants of equivalent 3–3 and 3–2 composites, respectively. In the transverse direction, $\bar{d}_{31}$ is given by

$$\bar{d}_{31}=\phi_{\text{ring}}d_{31,\text{PZT}}+\phi_{\text{trans}}d_{31,\text{trans}}+\phi_{\text{disk}}d_{31,\text{disk}}, \tag{13}$$

where $d_{31,\text{trans}}$ and $d_{31,\text{disk}}$ are the piezoelectric constants of equivalent 3–3 and 3–2 composites, respectively.

IV. RESULTS AND DISCUSSION

A. Structure of 3-*X* PZT–polymer composites

Representative 3-*X* composites produced via directed assembly are highlighted in Fig. 4. The top views of these composites illustrate the differences in their diameter due to removal of the perimeter ring. The cross-sectional views reveal the interior lattice structure present in all 3-*X* composites as well as the plate and ring elements contained in the 3–2 and 3–1 samples, respectively. These elements were intimately bonded to the interior structure. Such composites had a $\phi_{\text{PZT}}\sim 0.57$ within this lattice structure, which corresponded to an initial lattice (rod) spacing of 350 μm.

Sintered PZT skeletal structures used to fabricate 3–3 composites are shown in Fig. 5(a) with their perimeter ring intact. The ϕ_{PZT} and lattice spacing of each sample (1–8) in this array are summarized in Table III. The top surface of these PZT skeletal structures are illustrated in Figs. 5(b) and 5(c), which reveal the high degree of perfection in the PZT rod diameter and spacing within each structure. The cross-sectional view shown in Fig. 5(d) reveals the presence of PZT pillars formed by the intersections between rods. Clearly, the PZT phase exhibits excellent connectivity in all three directions. Analogous PZT skeletal structures were produced for the 3–2 and 3–1 composites, however, these are not shown since their internal structure is obscured by the presence of the face plate elements.

B. Properties of PZT monoliths and 3-*X* PZT–polymer composites

The dielectric constant (K_3), piezoelectric constants (d_{33} and d_{31}), and electromechanical coupling coefficients (k_P and k_{31}) determined for monolithic PZT disks are reported in Table IV. The properties of both robocast (RC) and cold isostatically pressed (CIP) disks exhibited good agreement with the reported properties for bulk PZT,[47] with variations of less than $\sim$7% observed. In addition, their $\tan\delta$ values were less than 0.025.

The dielectric constant ($\bar{K}_3$) of the 3-*X* PZT-polymer composites is plotted as a function ϕ_{PZT} in Fig. 6. The bar notation signifies that this property is an average value for the entire composite. ϕ_{PZT} represents the PZT volume fraction within the internal lattice structure rather than the total PZT content, which would be higher for both the 3–2 and 3–1 composites due to contributions from their face plate and ring elements, respectively. Each composite architecture displayed a similar monotonic decline of dielectric constant with decreasing ϕ_{PZT}. The dielectric constant of 3–1 composites was consistently higher than that observed for the other structures. Such differences become more noticeable at lower ϕ_{PZT}, where the neglected ring element contributed significantly to the overall permittivity. The dependence of

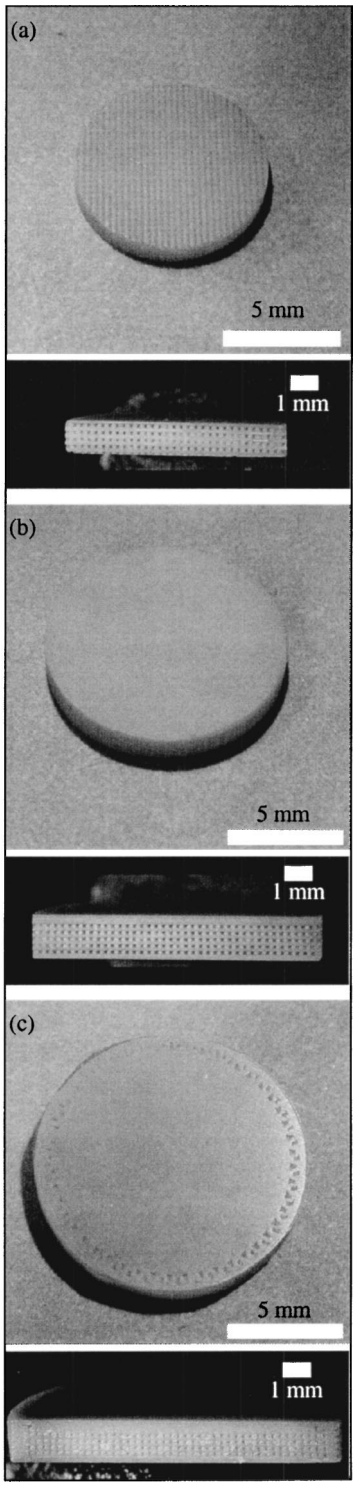

FIG. 4. Optical images of the top and cross-sectional views of (a) 3–3, (b) 3–2, and (c) 3–1 composites after polymer infiltration and machining. (Note: The ϕ_{PZT} in the lattice portion is ~0.6 for each sample.)

the dielectric constant on ϕ_{PZT} predicted using the isostrain, unit-cell models exhibited good agreement with these measured data. The dielectric constants for the 3–3 and 3–2 composites were lower than expected for $\phi_{PZT} > 0.5$, which likely arises from the simplifying assumption of rectangular PZT rod shape in the unit-cell model.

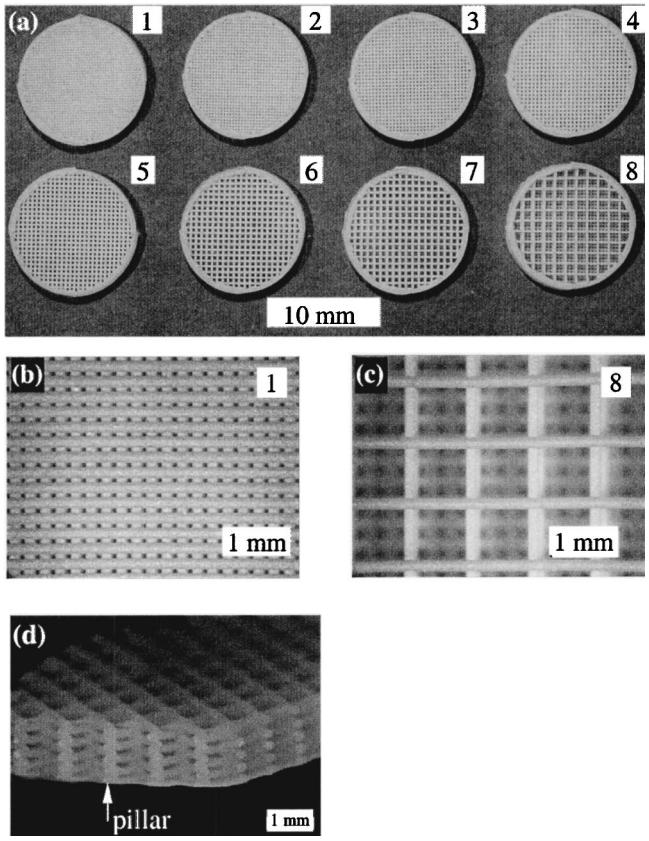

FIG. 5. Optical images of the densified PZT structures of varying lattice (rod) spacing, (b) and (c) top views of samples 1 and 8, respectively, and (d) cross-sectional view of sample 6.

The longitudinal piezoelectric constant ($\overline{d}_{33}$) of the 3-*X* composites is plotted in Fig. 7 as a function of ϕ_{PZT}. There was a similar reduction of $\overline{d}_{33}$ with decreasing ϕ_{PZT} for each composite architecture studied. The $\overline{d}_{33}$ values were higher for the 3–1 composites relative to the 3–3 composites, with the 3–2 composites displaying intermediate values. While the predicted $\overline{d}_{33}$ curves shown in Fig. 7 capture the general ϕ_{PZT} dependence, they were consistently higher than the measured data. We attribute such differences to the effects of nonuniform surface deflections. In related work, Cao and co-workers[30,31,43] have shown that the actual displacement profile is nonuniform for 2–2 and 1–3 composites, which leads to a stress concentration in the PZT pillars that is significantly less than predicted under the isostrain assumption.

TABLE III. Design of 3–3 composites.

Sample No.	Lattice spacing (μm)	ϕ_{PZT}
1	232	0.70
2	269	0.60
3	309	0.52
4	346	0.48
5	383	0.43
6	494	0.33
7	579	0.28
8	937	0.17

TABLE IV. Properties of PZT monolithic disks.

	K_{33}	d_{33} (pC/N)	d_{31} (pC/N)	k_p	k_{31}
PZT disks (RC)	3250	604	−269	−0.391	0.670
PZT disks (CIP)	3280	573	−255	−0.382	0.645
Reported values[a]	3400	593	−274	−0.388	0.650

[a]See Ref. 47.

This effect was exacerbated for thin composites, such as those studied here.[11,41,43] Rigid face plates have been shown to mitigate nonuniform surface deflections[43] and increase the efficiency of stress transfer to PZT pillars.[40,43] Thus, both the 3–2 and 3–1 composites were expected to exhibit improved stress transfer to the PZT pillars relative to the 3–3 composites, even so their measured values were still less than predicted by the unit-cell model. Interestingly, the $\overline{d}_{33}$ values measured for the 3–1 composites actually matched the predicted values obtained using the 3–2 model. This observation suggests that the ring element in the 3–1 composites contributes very little to their measured piezoelectric constant, which is perhaps reasonable given that the actual measurement conditions utilize a point contact to load the structures.

The hydrostatic piezoelectric constant ($\overline{d}_h$) for 3-*X* composites is plotted as a function of PZT volume fraction in Fig. 8. Similar trends were observed for all three composite architectures, with the 3–1 composites displaying the highest values $\overline{d}_h$ at a given ϕ_{PZT}. It is noteworthy that the 3–3 composites displayed a nearly equivalent (or lower) piezoelectric response to monolithic PZT over the compositional range studied. The measured $\overline{d}_h$ values for the 3–3 and 3–2 composites were less than predicted due to their lower $\overline{d}_{33}$ coefficients. Interestingly, the 3-1 composites exhibited higher $\overline{d}_h$ values than predicted by the 3–1 model. Such observations imply that under hydrostatic loading the $\overline{d}_{33}$ coefficient is enhanced, the $\overline{d}_{31}$ coefficient is diluted, or a combination of both occurs. A possible explanation for this

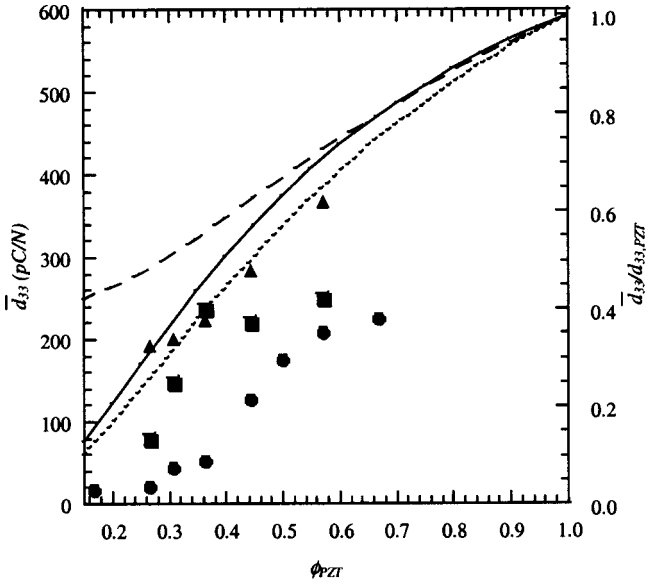

FIG. 7. Piezoelectric constant ($\overline{d}_{33}$) of 3–3 (●), 3–2 (■), and 3–1 (▲) composites as a function of PZT volume fraction (ϕ_{PZT}). The predicted $\overline{d}_{33}$ values from the iso-strain, unit-cell models are also shown for the 3–3 (solid curve), 3–2 (short-dashed curve), and 3–1 (long-dashed curve) composites, respectively. The secondary axis has been normalized to the piezoelectric constant of monolithic PZT.

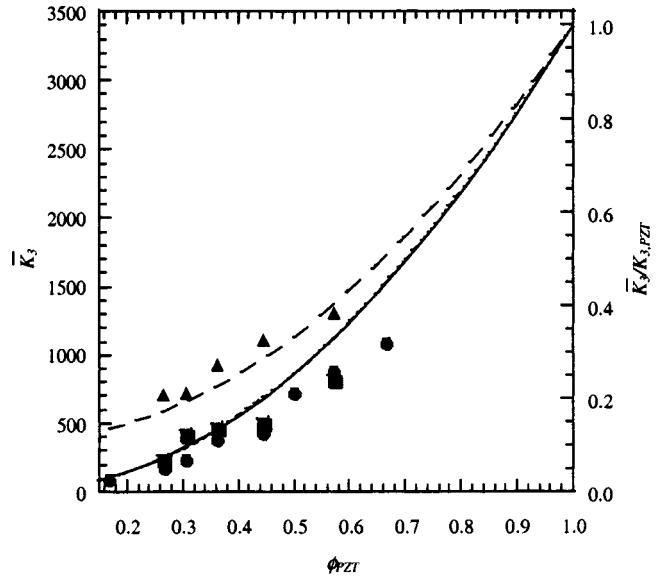

FIG. 6. Dielectric constant ($\overline{K}_3$) of 3–3 (●), 3–2 (■), and 3–1 (▲) composites as a function of PZT volume fraction (ϕ_{PZT}). The predicted $\overline{K}_3$ values from the iso-strain, unit-cell models are also shown for the 3–3 (solid curve), 3–2 (short dashed curve), and 3–1 (long-dashed curve) composites, respectively. Note, the $\overline{K}_3$ predictions of the 3–3 and 3–2 models are nearly indistinguishable such that the curves overlap. The secondary ordinate has been normalized to the dielectric constant of monolithic PZT.

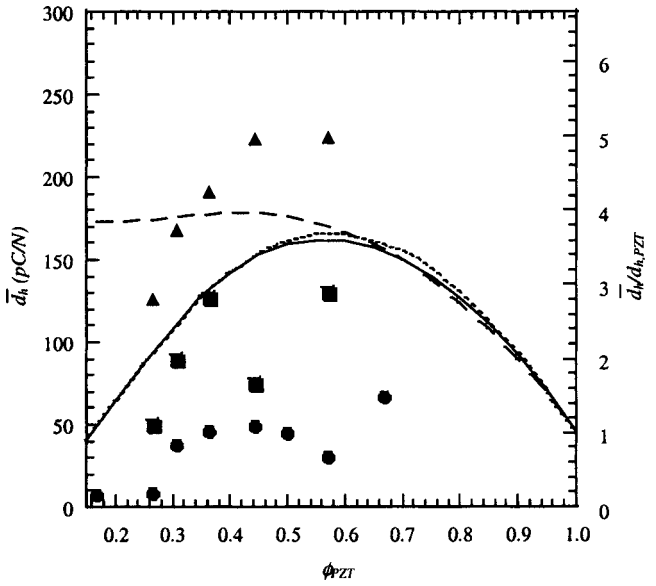

FIG. 8. Hydrostatic piezoelectric constant ($\overline{d}_h$) of 3–3 (●), 3–2 (■), and 3–1 (▲) composites as a function of PZT volume fraction (ϕ_{PZT}). The predicted $\overline{d}_h$ values from the iso-strain, unit-cell models are also shown for the 3–3 (solid curve), 3–2 (short-dashed curve) and 3–1 (long-dashed curve) composites, respectively. The secondary axis has been normalized to the hydrostatic piezoelectric constant of monolithic PZT.

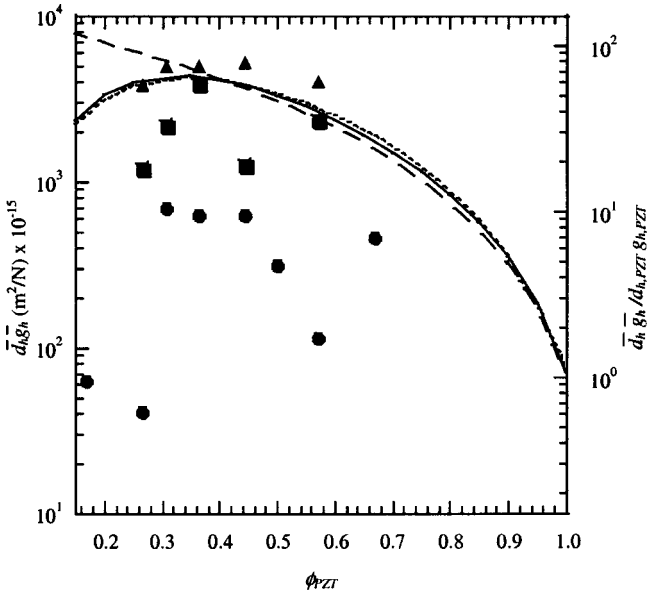

FIG. 9. Hydrostatic figure of merit ($\bar{d}_h\bar{g}_h$) for 3–3 (●), 3–2 (■), and 3–1 (▲) composites as a function of PZT volume fraction (ϕ_{PZT}). The predicted $\bar{d}_h$ values from the iso-strain, unit-cell models are also shown for the 3–3 (solid curve), 3–2 (short-dashed curve) and 3–1 (long-dashed curve) composites, respectively. The secondary axis has been normalized to the hydrostatic figure of merit of monolithic PZT.

stems from lateral stress shielding of the lattice that may occur in these composites due to presence of the face plates[40,43] and the ring element.[48] This type of shielding would lead to a diminished $\bar{d}_{31}$ and enhanced $\bar{d}_h$, which is not accounted for in our unit-cell models.

The hydrostatic figure of merit ($\bar{d}_h\bar{g}_h$) for these 3-*X* composites is plotted as a function of ϕ_{PZT} in Fig. 9, which was calculated using $\bar{g}_h=\bar{d}_h/\bar{K}_3\varepsilon_0$, where ε_0 is the permittivity constant. The 3–1 composites displayed the highest figures of merit with a maximum value of 4800 $\times 10^{-15}$ ($\mathrm{m^2\,N^{-1}}$) occurring at $\phi_{\mathrm{PZT}}\approx 0.45$. Both the 3–1 and 3–2 composites displayed ($\bar{d}_h\bar{g}_h$) values that exceeded those measured for monolithic PZT by at least an order of magnitude. Even the 3–3 composites displayed nearly a tenfold increase over monolithic PZT over a narrow compositional range ($\phi_{\mathrm{PZT}}\sim 0.31-0.45$), despite their lower $\bar{d}_h$ values. These measured values were also lower than the model predictions, which can be attributed to the effects described previously. Note, these 3-*X* composites exhibited figures of merit that were comparable to those reported for related PZT-polymer composites fabricated by alternate techniques.[2,7,13,49]

Our directed assembly approach offers a facile method for fabricating thin 3-*X* PZT/polymer composites over a wide compositional range and design space. Our future efforts will focus on further enhancing the performance of PZT-based composites. As a straightforward example, composites with an improved piezoelectric response could be engineered by utilizing a more compliant polymer (e.g., an elastomer).[7,9,41] In fact, given the flexibility of this fabrication method, 3–0 PZT-air composites that are fully encapsulated in a rigid PZT shell can be assembled. This architecture represents a simple modification of the 3–1 design, in which solid face plates extend all the way to the outer ring on the top and bottom surfaces. Using the multi-ink capabilities of the robotic deposition apparatus, fabrication of PZT-based composites with compositional variations along rods, between rods, or between layers in a given structure is also possible.

V. SUMMARY

3-*X* PZT-polymer composites were directly assembled via a robotic deposition technique, known as robocasting. Three types of composite architectures were fabricated including 3–3 PZT-polymer lattices, 3–2 structures with integrated faceplates, and 3–1 structures with integrated face plate and ring elements. Their dielectric and piezoelectric behavior was characterized over a broad compositional range (PZT: polymer ratio) and the results compared to predictions made using an isostrain, unit-cell model. The model predicted that the applied stress is largely supported by PZT pillars that lie parallel to the poling axis. The stress was not effectively transferred to these PZT pillars for the 3–3 lattices, because of nonuniform deflections on the exposed PZT-polymer surfaces. The addition of rigid PZT faceplates improved the stress transfer in the 3–2 and 3–1 architectures, resulting in a higher piezoelectric response for these thin composite structures. Our directed assembly route offers a promising approach for fabricating designer PZT-polymer composites needed for advanced hydrophone and ultrasonic sensors.

ACKNOWLEDGMENTS

The authors thank Q. Li and J. Stuecker for their experimental assistance, N. Sottos and D. Payne for valuable discussions, and S. Y. Lin for his support. In addition, we thank Professor Amar Bhalla of Pennsylvania State University for his assistance with the hydrostatic measurements. J.A. Lewis acknowledges partial support from the U.S. Department of Energy, Division of Materials Sciences through the Frederick Seitz MRL at UIUC. This work was funded by the National Science Foundation (Grant No. DMI 99-01030) and by Sandia, a multiprogram laboratory operated by Sandia Corporation, a Lockheed Martin Company, for the United States Department of Energy under Contract No. DE-AC04-94AL85000.

[1] R. E. Newnham, L. J. Bowen, K. A. Klicker, and L. E. Cross, Mater. Eng. **2**, 93 (1980).
[2] J. F. Tressler, S. Alkpu, A. Dogan, and R. E. Newnham, Appl. Sci. Manuf. **30A**, 477 (1999).
[3] V. F. Janas and A. Safari, J. Am. Ceram. Soc. **78**, 2945 (1995).
[4] T. R. Gururaja, Am. Ceram. Soc. Bull. **73**, 50 (1994).
[5] R. E. Newnham, D. P. Skinner, and L. E. Cross, Mater. Res. Bull. **13**, 525 (1978).
[6] R. E. Newnham, Proceedings of the 21st University Conference on Ceramic Science (1986), pp. 385–394.
[7] D. P. Skinner, R. E. Newnham, and L. E. Cross, Mater. Res. Bull. **13**, 599 (1978).
[8] T. R. Shrout, W. A. Schulze, and J. V. Biggers, Mater. Res. Bull. **14**, 1553 (1979).
[9] K. Rittenmyer, T. Shrout, W. A. Schulze, and R. E. Newnham, Ferroelectrics **41**, 189 (1982).
[10] A. Safari, R. E. Newnham, L. E. Cross, and W. A. Schulze, Ferroelectrics **41**, 197 (1982).

[11] A. Safari, A. Halliyal, and R. E. Newnham, Mater. Res. Bull. **17**, 301 (1982).
[12] T. Hayashi, S. Sugihara, and K. Okazaki, Ferroelectrics **131**, 75 (1992).
[13] M. J. Creedon and W. A. Schulze, Ferroelectrics **153**, 333 (1994).
[14] C. Van Hoy, A. Barda, M. Griffith, and J. W. Halloran, J. Am. Ceram. Soc. **81**, 152 (1998).
[15] M. Kahn and M. Chase, J. Am. Ceram. Soc. **75**, 649 (1992).
[16] M. Miyashita, K. Takano, and T. Toda, Ferroelectrics **28**, 397 (1980).
[17] M. Allahverdi, S. C. Danforth, M. Jafari, and A. Safari, J. Eur. Ceram. Soc. **21**, 1485 (2001).
[18] A. Bandyopadhyay, R. K. Panda, V. F. Janas, M. K. Agarwala, R. van Weeren, S. C. Danforth, and A. Safari, IEEE Trans. 999 (1996).
[19] D. B. Chrisey, Science **289**, 879 (2000).
[20] J. H. Song, M. J. Edirisinghe, and J. R. G. Evans, J. Am. Ceram. Soc. **82**, 3374 (1999).
[21] K. A. M. Seerden, N. Reis, J. R. G. Evans, P. S. Grant, J. W. Halloran, and B. Derby, J. Am. Ceram. Soc. **84**, 2514 (2001).
[22] S. L. Morissette, J. A. Lewis, P. G. Clem, J. Cesarano III, and D. B. Dimos, J. Am. Ceram. Soc. **84**, 2462 (2001).
[23] J. Cesarano III, R. Segalman, and P. Calvert, Ceram. Ind. **148**, 94 (1998).
[24] J. Cesarano III and P. Calvert, U.S. Patent No. 6,027,326.
[25] J. Cesarano III, Mater. Res. Soc. Symp. Proc. **542**, 133 (1998).
[26] E. Sachs, M. Cima, P. Williams, D. Brancazio, and J. Cornie, J. Eng. Ind. Trans. ASME **114**, 481 (1992).
[27] E. Sachs, M. Cima, J. Bredt, A. Curodeau, T. Fan, and D. Brancazio, Manuf. Rev. **5**, 117 (1992).
[28] M. Agarwala, A. Bandyopadhyay, R. van Weewn, A. Safari, S. C. Danforth, N. A. Langrana, V. R. Jamalabad, and P. J. Whalen, Am. Ceram. Soc. Bull. **75**, 60 (1996).
[29] B. A. Tuttle, J. E. Smay, J. Cesarano III, J. A. Voigt, T. W. Scofield, W. R. Olson, and J. A. Lewis, J. Am. Ceram. Soc. **84**, 872 (2001).
[30] W. Cao, Q. M. Zhang, and L. E. Cross, J. Appl. Phys. **72**, 5814 (1992).
[31] W. Cao, Q. M. Zhang, and L. E. Cross, IEEE Trans. Ultrason. Ferroelectr. Freq. Control **40**, 103 (1993).
[32] R. Buscall, P. D. A. Mills, J. W. Goodwin, and D. W. Lawson, J. Chem. Soc., Faraday Trans. 1 **84**, 4249 (1988).
[33] G. M. Channell and C. F. Zukoski, AIChE J. **43**, 1700 (1997).
[34] C. J. Rueb and C. F. Zukoski, J. Rheol. , 197 (1997).
[35] D. Stauffer, A. Coniglio, and M. Adam, Adv. Polym. Sci. **44**, 103 (1982).
[36] B. V. Velamakanni, F. F. Lange, F. W. Zok, and D. S. Pearson, J. Am. Ceram. Soc. **77**, 216 (1994).
[37] W. B. Russel, J. Rheol. **24**, 287 (1980).
[38] J. E. Smay, J. Cesarano III, and J. A. Lewis (unpublished).
[39] J. S. Reed, *Principles of Ceramics Processing*, 2nd ed. (Wiley, New York, 1995).
[40] N. M. Shorrocks, M. E. Brown, R. W. Whatmore, and F. W. Ainger, Ferroelectrics **54**, 215 (1984).
[41] K. A. Klicker, J. V. Biggers, and R. E. Newnham, J. Am. Ceram. Soc. **64**, 5 (1981).
[42] M. J. Haun, P. Moses, T. R. Gururaja, W. A. Schulze, and R. E. Newnham, Ferroelectrics **49**, 259 (1983).
[43] W. Cao, Q. M. Zhang, J. Z. ZHao, and L. E. Cross, IEEE Trans. Ultrason. Ferroelectr. Freq. Control **42**, 37 (1995).
[44] H. Banno, Proc. IEEE , 186 (1995).
[45] H. Banno, Jpn. J. Appl. Phys., Part 1 **33**, 5518 (1994).
[46] H. Banno, Jpn. J. Appl. Phys., Part 1 **32**, 4214 (1993).
[47] *Guide to Modern Piezoelectric Ceramics* (Morgan Matroc, Electroceramics Division, Bedford, OH, 1997).
[48] Q. M. Zhang, W. Cao, H. Wang, and L. E. Cross, J. Appl. Phys. **73**, 1403 (1993).
[49] M. J. Creedon, S. Gopalakrishnan, and W. A. Schulze, Proceedings of the IEEE International Symposium on Applications of Ferroelectrics, University Park, PA, August 7–10, 1994, pp. 299–302.